Computer Simulation of Solid State Transformation in Fe–C–Si Ternary Spheroidal Graphite Cast Iron

Ahmad Almansour[†], Kazuhiro Matsugi, Tomei Hatayama
and Osamu Yanagisawa

*Department of Materials Engineering, Faculty of Engineering, Hiroshima University,
1-4-1 Kagamiyama, Higashi-Hiroshima 739, Japan*

A model was developed to simulate the post-solidification process of Fe–C–Si spheroidal graphite (SG) cast iron. The calculated results at the end of solidification, like the nodule count, austenite shell radius, graphite volume fraction, graphite spheroid radius and silicon distribution in the austenite shell were considered to be the initial conditions for the post-solidification model. After the end the solidification, the graphite spheroid continues to grow due to the decrease of carbon solubility in the austenite. This growth of graphite in austenite was controlled by the carbon flux diffusing through graphite/austenite interface. The eutectoid transformation was also simulated. The rate constants and indexes of ferrite and pearlite formation in the Kolmogrov-Johnson-Mehl-Avrami's equation were modified from those which had been used for steel or SG cast iron in the literature. The growth of graphite during the eutectoid transformation was also investigated. The calculated results showed that about 50% of the graphite growth occurred after the end of solidification. The graphite growth that occurrs between eutectic equilibrium temperature and eutectoid equilibrium temperature occupies 40% of the total fraction and the rest 10% occurs during the eutectoid transformation. The calculated fractions of ferrite and pearlite agreed well with experimental result. Also from both the calculated and experimental results, it could be understood that the fraction of ferrite increased with decreasing part thickness.

I. Introduction

The simulation of solidification process has played a great role in the technology of spheroidal graphite cast iron. It helps predicting some characteristics of the casting, like shrinkage, hot spots locations and solidified microstructures. However, there are many materials-characteristics which cannot be determined at the end of solidification, because they change until lower temperatures after solidification. The mechanical properties of a casting are also strongly affected by the amount and distribution of phases which appear at relatively low temperatures like ferrite and pearlite. Therefore, it is important to establish a computational method to simulate the post-solidification phenomena.

The post-solidification phenomena in cooling process of SG cast iron include the growth of graphite in the austenite from the end of solidification to the eutectoid temperature and the eutectoid transformation: austenite (γ)→graphite + fertite (α) and/or austenite (γ)→pearlite.

Many attempts have been made to simulate the formation and growth of graphite during the whole cooling process. Skaland *et al.*[1] have developed a model which treated the growth of graphite in the post-solidification process. They have suggested that the growth is controlled by the difference in carbon concentration between the bulk austenite and the graphite/austenite interface.

The solid state transformation was also investigated by Lundbäck *et al.*[2] and Chang *et al.*[3] Nagasaka *et al.*[4] have developed a model to predict the microstructure of austempered ductile cast iron. They have calculated the volume fractions of bainite and martensite using TTT diagrams.

In the present work, the growth of graphite in austenite and the eutectoid transformation were investigated to predict the as-cast structure of SG cast iron. The nodule count, carbon and silicon concentrations, austenite grain size and volume fraction of graphite, which had been determined at the end of solidification, were used as the initial conditions for simulation of the solid state transformation.

II. The Model

1. Heat transfer and solidification kinetics

The governing equation for heat calculation is based on energy conservation and Fourier's laws, as eq. (1), and solved by a finite difference method with respect to time and position for the casting-mold system shown in Fig. 1.

$$\rho \cdot c_p \cdot \frac{\partial T}{\partial t} = \lambda \cdot \left(\frac{\partial^2 T}{\partial x^2} + \frac{\partial^2 T}{\partial y^2} + \frac{\partial^2 T}{\partial z^2} \right) + \rho \cdot L \cdot \frac{\partial f}{\partial t} \quad (1)$$

where ρ is the density, T is the temperature, c_p is the specific heat, λ is the heat conductivity, L is the latent heat of solidification or transformation, f is the fraction

---
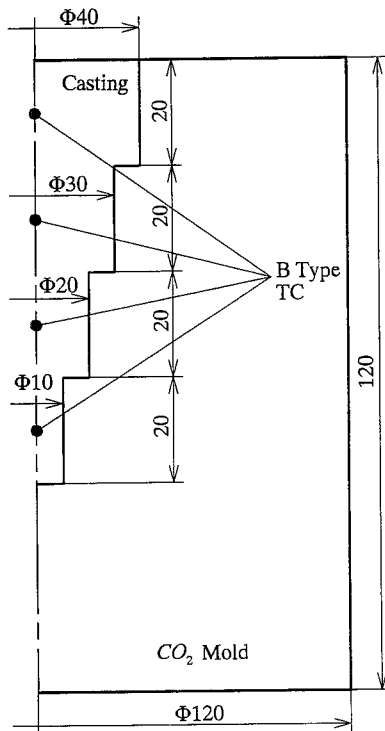
[†] Graduate Student, Hiroshima University.

Fig. 1 Schematic of the mold-casting system showing the insertion points of the thermocouples.

Table 1 Calculated results of the center of each step at the end of solidification.

Condition	Φ10	Φ20	Φ30	Φ40
Graphite volume fraction (%)	8.3	9.6	9.1	8.2
Nodule count/m³	50000·10⁹	24500·10⁹	19750·10⁹	14100·10⁹
Radius of austenite shell, r_γ/m	28.2·10⁻⁶	36.4·10⁻⁶	38.8·10⁻⁶	43.0·10⁻⁶
Radius of graphite spheroid, r_g/m	7.44·10⁻⁶	9.93·10⁻⁶	10.5·10⁻⁶	11.3·10⁻⁶

solidified or transformed, and t is the time.

The growth in the solidification process is controlled by the diffusion of carbon in the austenite shell. More details on the heat calculation, nucleation and growth model in the solidification process are given in Ref. (5).

It should be noted that the calculated results at the end of solidification, like nodule count, austenite shell radius, graphite volume fraction, graphite spheroid radius and silicon distribution in austenite shell are considered to be the initial conditions for the post-solidification model. These results are listed in Table 1 for the center of each step of the casting as an example. Also the distributions of silicon and carbon in austenite shell at the end of solidification are shown in Fig. 2 as an example.

2. Graphite growth in austenite

Even after the solidification is completed, the graphite nodules continue to grow due to the decrease of carbon
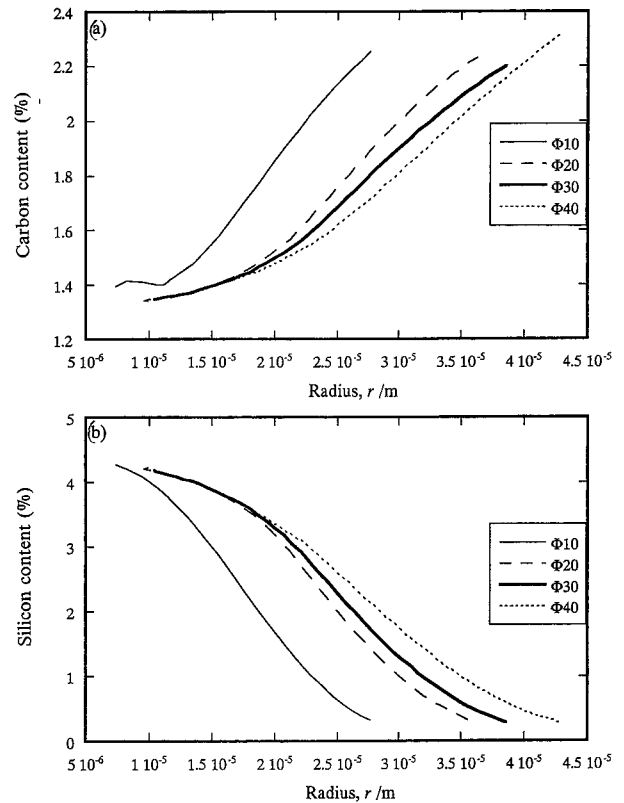

Fig. 2 The calculated distribution of (a) carbon and (b) silicon in the austenite shell at the center of each step in casting at the end of solidification.

solubility in the austenite. This growth is controlled by the amount of carbon flux diffusing through graphite/austenite interface. Assuming that the amount of carbon rejected from the austenite is equal to that diffuses to the graphite, the following mass balance equation can be derived:

$$\rho_\gamma \cdot S_g \cdot D_C^\gamma \cdot \frac{\partial C}{\partial r}\bigg|_{r=r_g} \cdot \Delta t = \rho_g \cdot S_g \cdot \Delta r_g \cdot 100 \qquad (2)$$

where C is the concentration of carbon in mass%, ρ_γ is the density of austenite, D_C^γ is the diffusivity of carbon in austenite, S_g is the surface area of graphite in contact with austenite, ρ_g is the density of graphite and Δr_g is the increment of graphite radius in time step Δt. Concerning the grain impingement, S_g is given by eq. (3) using the Kolgomorov-Johnson-Mehl-Avrami (KJMA) assumption,

$$S_g = (1 - f_g) \cdot 4\pi \cdot r_g^2 \cdot N \qquad (3)$$

where f_g is the volume fraction of the graphite nodule and N is the nodule count of graphite in unit volume.

Table 2 shows the values of the physical properties and other parameters used in the model. In eq. (2) the concentration gradient is calculated by assuming that carbon distribution through the austenite shell is presented by eq. (4), which is the solution on the quasi-steady state assumption[6], as shown in Fig. 3.

Table 2   The physical properties and other parameters used in the model.

Time step	0.01 s
$D_C^{\gamma(9)}$	$D_0\,(\mathrm{m^2/s})=1.75\cdot10^{-6}$ $Q\,(\mathrm{J/mol})=113462$
$\rho_g^{(10)}$	$1710\,\mathrm{Kg/m^3}$
$\rho_\gamma=\rho_\alpha$	$7270\,\mathrm{Kg/m^3}$
Solubility limit surface equation[11]	$T\,(^\circ\mathrm{C})=5.5\cdot(C_{\mathrm{Si}}^{\gamma/g}+1.1)^2+731.3$ $\quad+\dfrac{-5.5\cdot C_{\mathrm{Si}}^{\gamma/g^2}-9.7\cdot C_{\mathrm{Si}}^{\gamma/g}+415.045}{1.33-0.169\cdot C_{\mathrm{Si}}^{\gamma/g}}\cdot(C_C^{\gamma/g}-0.68+0.029\cdot C_{\mathrm{Si}}^{\gamma/g})$
$C_C^{\gamma/\alpha(7)}$	$=5.203-0.00614\cdot T+0.1665\cdot C_{\mathrm{Si}}^{\gamma/\alpha*1}$
$C_C^{\alpha/\gamma(11)}$	$=0.1063-0.00012\cdot T+0.0131\cdot C_{\mathrm{Si}}^{\alpha/\gamma*1}$
$C_C^{\alpha/g(12)(13)}$	$=2587\cdot\exp\left(-0.53\cdot C_{\mathrm{Si}}^{\alpha/g}-\dfrac{12110}{T}\right)^{*2}$
$k_f'^{(14)}$	$=\exp(-0.0145\cdot\Delta T+3.98\cdot\ln\Delta T-5.39\cdot\%C-16.5)^{*3}$
$k_p'^{(14)}$	$=\exp[-41.5\cdot\Delta T^{0.0723}\cdot e^{-0.0364\cdot\Delta T}]$
$n_f^{(14)}$	1
$n_p^{(15)}$	3
Latent heat of formation of ferrite and pearlite	Fig. 1 in Ref. (16)

*1   The temperature in the equation is given by °C.
*2   The temperature in the equation is given by K.
*3   %C is carbon content which is assumed to be the carbon content at S' in ternary phase diagram. $\%C=0.68-0.029\cdot C_{\mathrm{Si}}^{0.(7)}$.
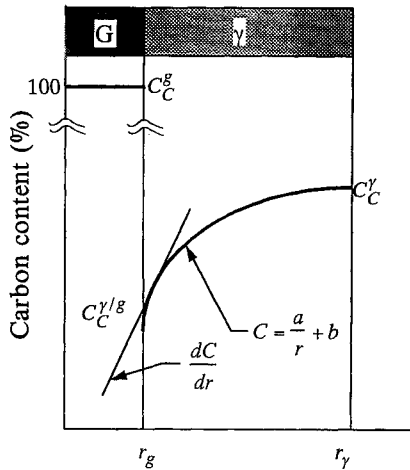

Fig. 3   Schematic of carbon concentration distribution in austenite shell after the end of solidification.

$$C=\frac{a}{r}+b \qquad (4)$$

where a and b are constants and can be calculated if the boundary conditions are known. The first derivative of eq. (4) at the graphite/austenite interface ($r=r_g$) will be as follows:

$$\left.\frac{\partial C}{\partial r}\right|_{r=r_g}=-\frac{a}{r_g^2} \qquad (5)$$

By substituting eq. (5) in eq. (2) and rearranging, the increment of graphite radius can be expressed by

$$\Delta r_g=\frac{\rho_\gamma}{\rho_g}\cdot\frac{1}{100}\cdot D_C^\gamma\cdot\left(-\frac{a}{r_g^2}\right)\cdot\Delta t$$

$$a=\frac{r_g\cdot r_\gamma}{r_g-r_\gamma}(C_C^\gamma-C_C^{\gamma/g}) \qquad (6)$$

The carbon concentration, $C_C^{\gamma/g}$, at the graphite/austenite interface is calculated directly from the equation of the carbon solubility limit surface in the ternary phase diagram shown in Fig. 4(a). Figure 4(b) schematically shows the related compositions using a binary Fe–C phase diagram for simplicity. When temperature decreases, $C_C^{\gamma/g}$ decreases along the solubility surface. At the same time the average carbon concentration in the austenite decreases by the growth of graphite. This variation can be presented by the following integral equation assuming that the amount of carbon rejected from the austenite causes the radius of graphite spheroid to grow by the amount of Δr_g:

$$\rho_\gamma\cdot\int_{r_g}^{r_\gamma}C\cdot\mathrm{d}f^{t+\Delta t}=\rho_\gamma\cdot\int_{r_g}^{r_\gamma}C\cdot\mathrm{d}f^t-\rho_g\cdot S_g\cdot\Delta r_g\cdot100 \qquad (7)$$

where r_γ is the outer radius of austenite shell having no regard to grain impingement of austenite and f is the volume fraction corresponding to radius r. In eq. (7) $\mathrm{d}f$ is calculated according to the KJMA assumption as follows:

$$\mathrm{d}f=4\pi Nr^2\cdot\exp\left(-\frac{4}{3}\pi Nr^3\right)\cdot\mathrm{d}r \qquad (8)$$

Substituting eqs. (4) and (8) in eq. (7) gives

$$\rho_\gamma\int_{r_{g1}}^{r_\gamma}r^2\left(\frac{a_1}{r}+b_1\right)\exp\left(-\frac{4}{3}\pi Nr^3\right)\mathrm{d}r=$$

$$\rho_\gamma\int_{r_{g0}}^{r_\gamma}r^2\left(\frac{a_0}{r}+b_0\right)\exp\left(-\frac{4}{3}\pi Nr^3\right)\mathrm{d}r$$

$$-(1-f_{g1})\cdot r_{g1}^2\cdot\Delta r_g\cdot\rho_g\cdot100 \qquad (9)$$

$$a_0=\frac{r_{g0}\cdot r_\gamma}{r_{g0}-r_\gamma}(C_{C0}^\gamma-C_{C0}^{\gamma/g})\quad b_0=\frac{r_{g0}\cdot C_{C0}^{\gamma/g}-r_\gamma\cdot C_{C0}^\gamma}{r_{g0}-r_\gamma}$$
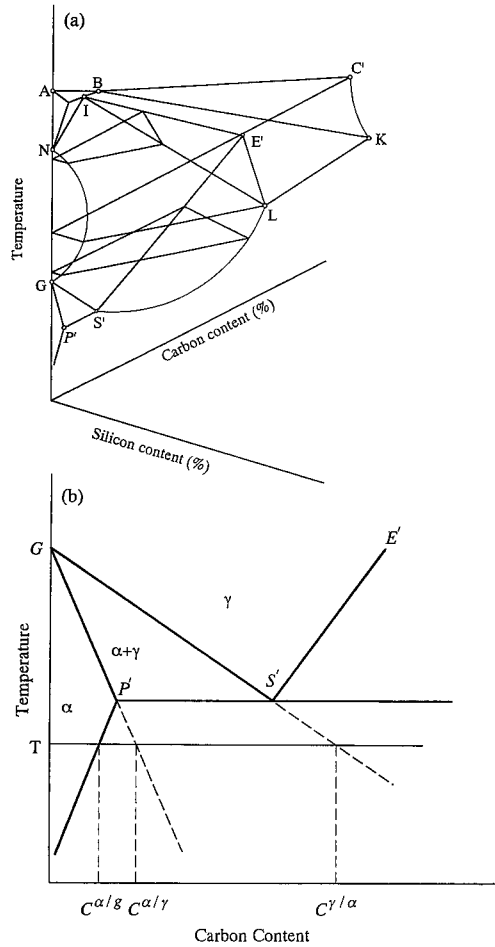
Fig. 4 (a) A part of Fe-C-Si ternary phase diagram and (b) binary schematic illustrates the compositions at different interfaces.

$$a_1 = \frac{r_{g1} \cdot r_\gamma}{r_{g1} - r_\gamma} (C_{C1}^\gamma - C_{C1}^{\gamma/g}) \quad b_1 = \frac{r_{g1} \cdot C_{C1}^{\gamma/g} - r_\gamma \cdot C_{C1}^\gamma}{r_{g1} - r_\gamma} \quad (10)$$

In eqs. (9) and (10) the indexes 0 and 1 designate the values at time t and $t + \Delta t$ respectively. C_{C1}^γ is calculated after rearranging eq. (9) and solving the integrations by the Simpson's numerical method.

3. Eutectoid transformation

(1) Region below eutectoid temperature

When the austenite is cooled below the A_1 temperature, a eutectoid reaction may occur, which includes austenite→ferrite+graphite or austenite→pearlite transformations. The equilibrium transformation temperature is calculated in the Fe-C-Si ternary system by the following equation[7]:

$$T_{A1} = 5.5 \cdot (C_{Si}^S + 1.1)^2 + 731.3 \quad (11)$$

Silicon segregation occurs during solidification, resulting in an inhomogeneous concentration distribution in the austenite shell, where the silicon concentration is higher at the graphite/austenite interface and lower at the austenite shell boundary. Therefore, as known by eq. (11), not all areas in the austenite shell are ready for the eutectoid transformation to occur at the same tempera-
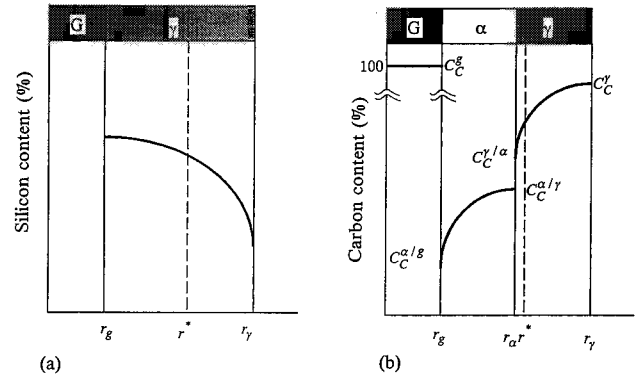

Fig. 5 (a) The definition of the critical radius and (b) the distribution of carbon concentration during eutectoid transformation.

ture. The part of austenite shell which will be a place for eutectoid transformations is bounded by the dashed line in Fig. 5. Here the critical radius, r^*, coincides with eutectoid transformation temperature and hence all areas out of this radius will have temperatures higher than T_{A1} at which no transformation occurs. The critical radius is calculated as follows. The silicon concentration C_{Si}^S at radius r in the austenite shell, which was determined in solidification process[5], is assumed to be presented by the Scheil equation,

$$C_{Si}^S = k_0^{Si} \cdot C_{Si}^L = k_0^{Si} \cdot C_{Si}^0 \cdot (1-f)^{k_0^{Si}-1}$$

$$= k_0^{Si} \cdot C_{Si}^0 \cdot \exp\left[-\frac{4}{3} \cdot \pi \cdot (r^{*3} - r_g^3) \cdot N \cdot (k_0^{Si}-1) \right] \quad (12)$$

where C_{Si}^0 is the initial concentration of silicon and k_0^{Si} is the redistribution coefficient in solidification process. After C_{Si}^S is calculated from eq. (11) at an arbitrary temperature, the critical radius can be given as eq. (13) from eq. (12).

$$r^* = \sqrt[3]{\frac{\ln\left(\dfrac{C_{Si}^S}{k_0^{Si} \cdot C_{Si}^0}\right)}{-\dfrac{4}{3} \cdot \pi \cdot N \cdot (k_0^{Si}-1)} + r_g^3} \quad (13)$$

(2) Eutectoid transformation

The amount of solid phase transformed X_j is calculated using the KJMA equation,

$$X_j = 1 - \exp(-k_j t^{n_j}) \quad (14)$$

where k is rate constant and n is rate index and j designates ferrite when j is f or pearlite when j is p. The growth rates of pearlite and ferrite are determined as eqs. (15) and (16) from eq. (14).

$$\frac{dX_p}{dt} = k_p n_p \left\{ -\frac{1}{k_p} \ln(1-X_p) \right\}^{n_p-1/n_p} (1-X_f-X_p) \quad (15)$$

$$\frac{dX_f}{dt} = k_f n_f \left\{ -\frac{1}{k_f} \ln(1-X_f) \right\}^{n_f-1/n_f} (1-X_f-X_p) \quad (16)$$

In steel alloys the rate constant is known to be dependent on the nucleation rate and growth rate[8] and is

influenced by the diameter of the original austenite grain. This may be applied to steel alloys where the ferrite forms at austenite grains boundaries. The ferrite is considered to form at the graphite/austenite interface due to the depletion of carbon by graphite growth in the case of SG cast iron. Therefore, the effect of g/γ interface area can be considered instead of austenite grain diameter in this case. Accordingly, the rate constant of ferrite is assumed to be a function of g/γ interface area in the present work:

$$k_f = k_f' \cdot F(S_g) \tag{17}$$

where k_f' is the rate constant of ferrite in the KJMA equation without including S_g effect and $F(S_g)$ is a function of g/γ interface area S_g. On the other hand, it is presumed that pearlite forms at ferrite/austenite interface and hence the rate constant k_p is assumed to be a function of the ferrite shell surface area S_α.

$$k_p = k_p' \cdot F(S_\alpha) \tag{18}$$

where k_p' is the rate constant of pearlite in the KJMA equation without including S_α effect and $F(S_\alpha)$ is a function of S_α which changes during the transformation. The values of k_f', k_p', n_f and n_p used in this calculation are shown in Table 2.

In calculating the volume fraction of ferrite and pearlite, the fact that not all of austenite shell will participate in eutectoid transformation should be considered. Therefore, the volume increments of ferrite and pearlite are first calculated with respect to the volume in which the temperature is below the eutectoid and then they are converted to bulk volumes so that the ferrite shell radius should not exceed the critical radius calculated from eq. (13).

During the quasi-steady state growth, the amount of carbon which diffuses down the concentration gradient away from the γ/α interface is balanced by the amount of carbon absorbed by graphite nodule. Therefore, the following mass balance equation is applied to the ferrite shell:

$$\rho_g \cdot S_g \cdot (100 - C_C^{\alpha/g}) \cdot \Delta r_g = \rho_\alpha \cdot S_\alpha \cdot (C_C^{\gamma/\alpha} - C_C^{\alpha/\gamma}) \cdot \Delta r_\alpha \tag{19}$$

where S_g is the surface area of graphite in contact with ferrite, ρ_α is the density of ferrite, S_α is the surface area of ferrite in contact with austenite, and Δr_α is the radius increment of ferrite shell. The concentrations are shown in Fig. 5(b) and calculated from Fe–C–Si ternary phase diagram as listed in Table 2. By rearranging eq. (19), the radius increment of graphite nodule is given by eq. (20):

$$\Delta r_g = \frac{\rho_\alpha}{\rho_g} \cdot \frac{S_\alpha}{S_g} \cdot \frac{(C_C^{\gamma/\alpha} - C_C^{\alpha/\gamma})}{(100 - C_C^{\alpha/g})} \cdot \Delta r_\alpha \tag{20}$$

III. Experimental Procedures

The melt was treated with 1% nodularizer and 0.2~0.3% inoculant, the chemical compositions of which are shown in Tables 3 and 4, respectively. As shown in Fig. 1, B type thermocouples (Pt-6Rh/Pt-30Rh) were

Table 3 Chemical composition of the nodularizer.

Mg	Si	Ca	RE	Al
4.78	45.83	1.95	1.97	0.39

Table 4 Chemical composition of the inoculant.

Si	Ca	Al	Fe
75.20	1.43	2.29	Bal.

Table 5 Chemical composition of SG cast iron.

Fe	Mg	C	Si	Mn	P	S	Cr
Bal.	0.038	3.51	2.69	0.37	0.018	0.009	0.03

placed at the center of each step to determine the cooling curves. The thermocouple wires (0.3 mm in dia.) were insulated by a twin hole alumina sheath and this in turn was protected by a silica sheath of 3.2 mm inner diameter and 4.0 mm outer diameter. The melt was poured into CO_2 mold and cooled to the room temperature in the mold. The chemical composition of the produced SG cast iron is shown in Table 5. The casting was cut vertically at the center and then the specimen was prepared for metallographical examination. An image analyzing system (IAS) was used to measure the nodule count over the whole section. The ferrite volume fraction was considered equal to the ferrite area fraction measured by IAS. The pearlite volume fraction was taken as the balance.

IV. Results and Discussion

The amount of heat released during the formation of ferrite and pearlite was considered in calculation and the temperature elevation in eq. (1) due to phase transformation was calculated as $\Delta T_j = (L_j/c_j) \cdot \mathrm{d}f_j$, where j indicates ferrite or pearlite, c is specific heat, $\mathrm{d}f$ is volume increment of phase j and L is latent heat of transformation. In the present model the latent heats of formation of ferrite and pearlite and the specific heat were taken as functions of temperature[16]. Figure 6 shows the calculated cooling curves at the center of each step compared with the experimental ones. The agreement between the two results is quite obvious except at the center of the step of 10 mm in diameter. The reasons for this disagreement for the step of 10 mm in diameter are described in Ref. (5).

Figure 7 shows the variation of graphite spheroid radius and graphite volume fraction with time for the center of each step of the casting. The growth of graphite was divided into three stages: solidification, graphite growth in the temperature range between eutectic and eutectoid and finally eutectoid transformation. In Fig. 7, A, B and D designate the start of solidification, the end of solidification, and the time at which the equilibrium
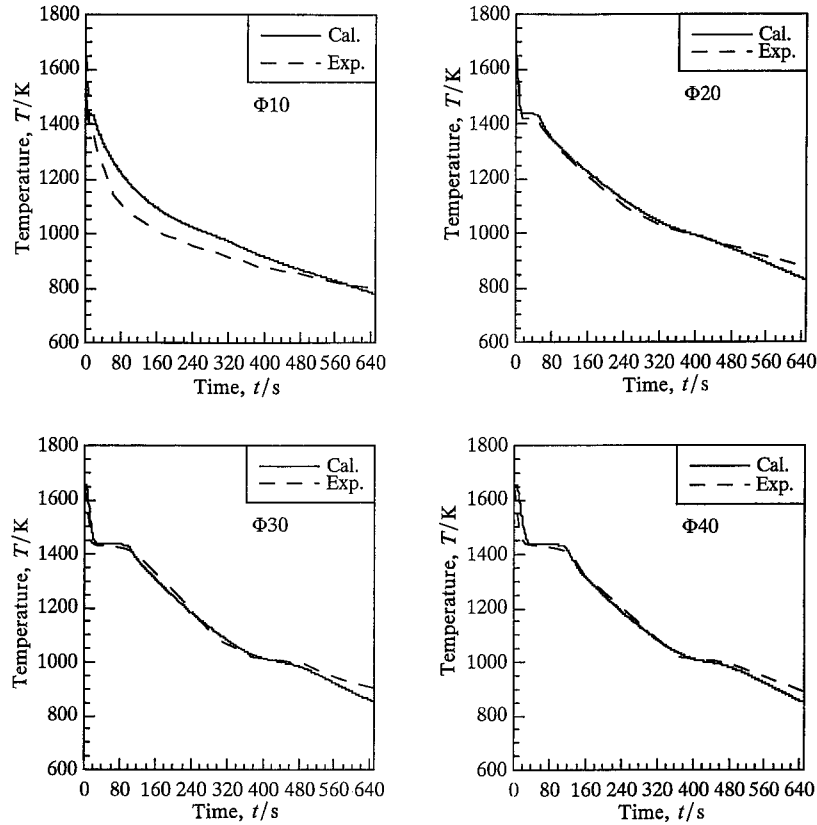
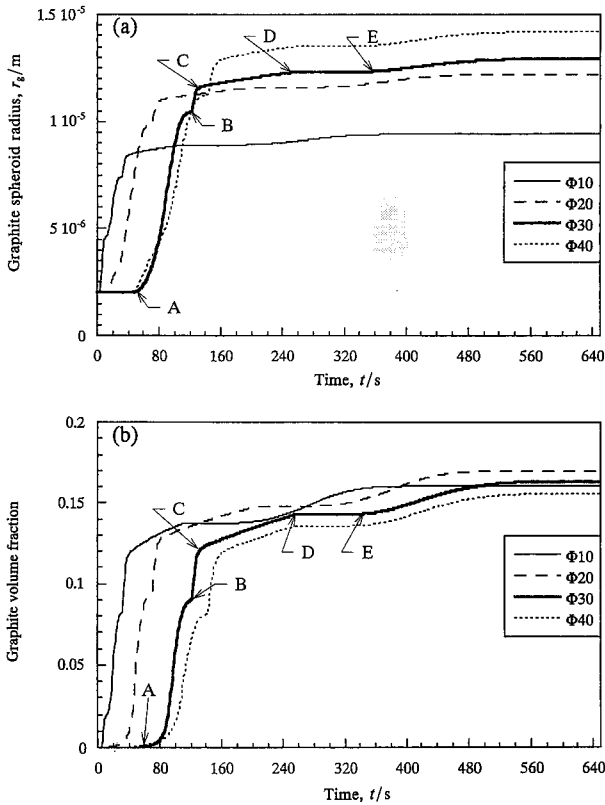Fig. 6 Calculated and experimental cooling curves for the center of each step.

Fig. 7 The variation of (a) graphite spheroid radius and (b) graphite volume fraction with time, during the whole cooling process for the center of each step.

eutectoid transformation temperature at the graphite/austenite interface was reached, respectively. Although the growth rate of graphite became slower at the final stage of solidification, it increased abruptly once the solidification finished at B. This behavior may be explained by the difference in carbon concentration between C_C^{γ} and $C_C^{\gamma/g}$. At the beginning of the stage between B and C, the difference in concentration was quite large and therefore the concentration gradient at austenite/graphite interface was also large, causing the accelerated graphite growth. However, this difference became smaller as the graphite growth proceeded and the concentration gradient at γ/g interface decreased and hence the growth rate began to decrease at C. After C to D, the amount of graphite growth is not so large in spite of the decrease in $C_C^{\gamma/g}$, because the diffusivity of carbon, D_C^{γ} in eq. (6), decreases as the temperature decreases. After the equilibrium eutectoid transformation temperature was reached at D, the growth rate of graphite was insignificant. But it increased after E which designates the start of ferrite formation. This can be understood by referring to eq. (20). In the region between D and E, although the equilibrium temperature was reached, the formation of ferrite was very slow resulting in slow growth of graphite.

The calculated results at the end of each stage are shown in Table 6. Comparing the volume fraction of graphite at the end of each stage with that at room temperature, almost 50% of graphite growth occurred after

Table 6   Graphite spheroid radius and volume fraction for the center of each step at different stages of the process.

		Graphite sheroid radius, r_g/m				Graphite volume fraction, f_g/%			
		Φ10	Φ20	Φ30	Φ40	Φ10	Φ20	Φ30	Φ40
Calculation	At the end of solidification	$7.44 \cdot 10^{-6}$	$9.93 \cdot 10^{-6}$	$10.5 \cdot 10^{-6}$	$11.3 \cdot 10^{-6}$	8.3	9.6	9.1	8.2
	Before eutectoid trans. starts	$8.90 \cdot 10^{-6}$	$11.6 \cdot 10^{-6}$	$12.3 \cdot 10^{-6}$	$13.5 \cdot 10^{-6}$	13.7	14.8	14.3	13.6
	At room temperature	$9.42 \cdot 10^{-6}$	$12.2 \cdot 10^{-6}$	$12.9 \cdot 10^{-6}$	$14.2 \cdot 10^{-6}$	16.1	17.0	16.4	15.6
Experiment	At room temperature	$13.5 \cdot 10^{-6}$	$17.6 \cdot 10^{-6}$	$17.5 \cdot 10^{-6}$	$19.8 \cdot 10^{-6}$	12.0	14.0	16.0	12.0

the end of solidification, 40% of which was the growth in the austenite and the rest 10% occurred during the eutectoid transformation. It can be also noticed that the growth of graphite during eutectoid transformation is not so large comparing to other two stages. This is because when the ferrite shell grows around the graphite spheroid, the diffusion distance for carbon atoms becomes longer. The coarsening of graphite spheroid at small cooling rates (thick parts) was balanced by the increase of nodule count at higher cooling rates (thin parts), and hence the volume fraction of graphite did not vary too much with thickness. Both the calculated and experimentally measured graphite volume fractions were 12–17% at room temperature.

Figure 8 shows the variation with time of both ferrite

and pearlite fractions for the center of each step. Simulated and experimental data for the fraction of phases are given in Table 7. The rate constants listed in Table 2 were actually used by Campbell et al. for the treatment of steel[14]. There are some problems in using the same parameters for the calculation of SG cast irons. The parameters had to be modified to fit the eutectoid trans-

Table 7   Calculated and experimental ferrite/pearlite fractions.

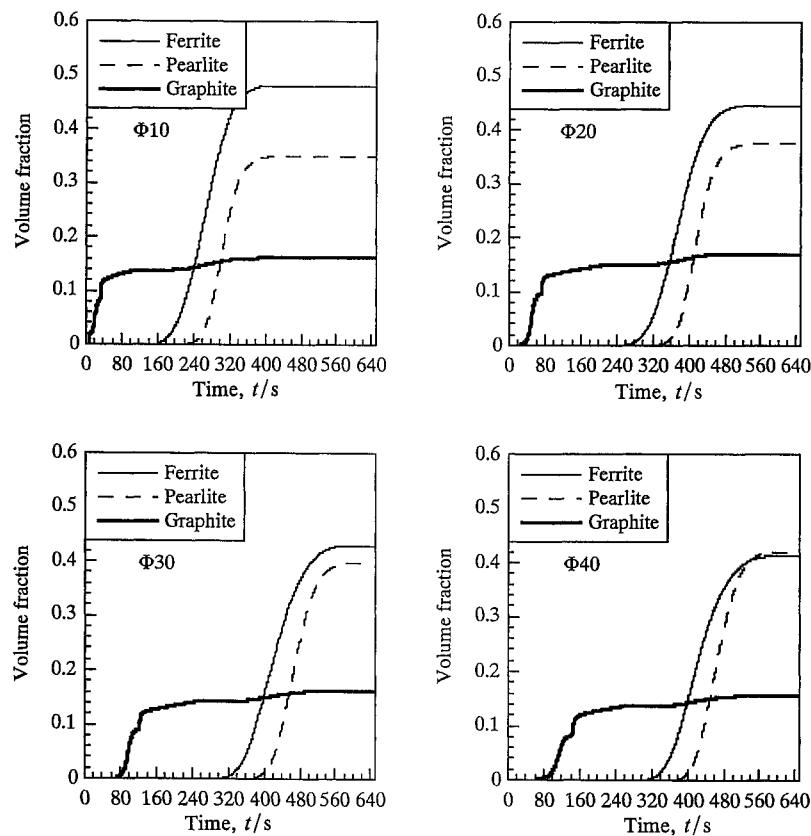| Step dia.	Φ10	Φ20	Φ30	Φ40
Calculated	48.9/35	45/38	43/40.6	41/43.4
Experimental	61/27	45/41	43/41	40/48

Fig. 8   The ferrite, pearlite and graphite evolution as a function of time for the center of each step.

formation of SG cast iron, because the equilibrium eutectoid transformation temperature of SG cast iron was higher than that in steel alloys. This can be simply related to the silicon content as shown in eq. (11). The average silicon content in the steel alloys used by Campbell *et al.* was about 0.22% which is far lower than the value used in the present work. Therefore, the rate constants had to be adjusted to cover the difference in transformation temperature because they are known to be strongly sensitive to temperature. Another reason was that the formation sites of ferrite and pearlite in SG iron should be much different from steel. The ferrite was supposed to have formed in the carbon depleted zone that surrounds the graphite spheroid. This fact has led us to include the effect of graphite spheroids surface area on the rate constant value. On the other hand, the pearlite was presumed to start forming at the austenite/ferrite interface. Therefore, the influence of α/γ surface area had to be included in calculating the rate constant of pearlite formation. As a result, the function $F(S_g)$ in eq. (17) was assumed to be equal to $(8.0 \cdot 10^{-3} \cdot S_g)$, and the function $F(S_\alpha)$ in eq. (18) was assumed to be equal to $(4.0 \cdot 10^{-7} \cdot S_\alpha)$. To calculate k_f' and k_p' by the equations shown in Table 2, the undercooling had to be known. At the critical radius there is no undercooling and at g/α interface the undercooling is maximum. In the present model the undercooling was taken as the average of the undercoolings at both interfaces. It can be also noticed from Fig. 8 that the start of pearlite formation delayed from the start of fertite formation. During calculation this fact can be explained by the behavior of S_α. At the beginning of ferrite formation S_α was small, then it increased with ferrite shell growth giving the chance for pearlite to start forming at α/γ interface. The value of n_f was taken as the round number of the average value used by Campbell *et al.*[14], whereas the value of n_p was chosen assuming the site saturation[15].

Generally, during ferrite formation two factors competitively participate in determining the amount of transformed ferrite. These factors are nodule count and structure coarseness. Lalich *et al.*[17] have reported that ferrite content increases with increase in nodule count in continuously cooled SG cast iron. Venugopalan[18] noted that the same effect of nodule count on ferrite content had to exist in isothermal transformation condition. It can be understood from Table 7 that ferrite fraction decreases with increasing part thickness or in other words increases with the increase in nodule count. This effect was relatively well predicted in the simulated results, although many assumptions were included in this model.

V. Conclusions

The growth of graphite in austenite and the eutectoid transformation were studied. In austenite the growth of graphite was assumed to be controlled by the diffusion of carbon through graphite/austenite interface. It was understood as the result of the calculation that 40% of graphite growth occurred during this stage. During eutectoid transformation the graphite continued to grow. This was controlled by the rate at which carbon diffuses from austenite to graphite through the ferrite shell. This growth was calculated to have covered 10% of the final fraction. The formation of ferrite and pearlite was also investigated. The rate constants of ferrite and pearlite formation, which had been originally developed for steel alloys, were modified to fit the eutectoid transformation of SG cast iron in the present work. As a result it was observed that ferrite fraction decreased with increasing part thickness.

REFERENCES

(1) T. Skaland, Ø. Grong and T. Grong: Metall. Trans. A, **24A** (1993), 2347.
(2) E. Lundbäck, I. Svensson and P. E. Persson: *Proc. Modelling of Metal Forming Process*, ed. by J. L. Chenot *et al.*, Kluwer Academic Publishers, (1988), p. 37.
(3) S. Chang, D. Shangguan and D. M. Stefanescu: Metall. Trans. A, **23A** (1992), 1333.
(4) Y. Nagasaka, M. Nachi, S. Kiguchi and I. Ohnaka: Imono, **64** (1992), 462.
(5) A. Almansour, K. Matsuki, T. Hatayama and O. Yanagisawa: Mater. Trans., JIM, **36** (1995), 1487.
(6) P. G. Shewmon: *Diffusion in Solids*, ed. by M. B. Bever *et al.*, McGraw-Hill Series in Materials Science and Engineering, (1963), p. 21.
(7) H. Nieswaag, J. W. Nijhof: *Mat. Res. Soc. Symp. Proc.*, ed. by H. Fredriksson *et al.*, Elsevier Science Publishing, **34** (1985), p. 411.
(8) *Thermomechanical Behavior of Materials during Transformation—Theory and Numerical Simulation*—ed. by Japan Society of Mechanical Engineers, Corona Publishing Co., Ltd., Tokyo, (1991), p. 45.
(9) D. F. Kalinovich, I. I. Kovenskii and M. D. Smolin: Izv. Vyssh. Ucheb. Fiz, **9** (1971), 116.
(10) W. D. Wood and H. W. Deem: *Thermal properties of high-temperatures materials*, Battelle Memorial Institute Columbus, Ohio, (1968), p. 214.
(11) E. Schurmann and J. von Hirsch: Giesserei techn.-wiss. Beihefte, **18** (1966), 1.
(12) T. Nishizawa: Bulletin Japan Inst. Metals, **12** (1973), 322.
(13) T. Nishizawa: Bulletin Japan Inst. Metals, **12** (1973), 401.
(14) P. C. Campbell, E. B. Hawbolt and J. K. Brimacombe: Metall. Trans. A, **22A** (1991), 2779.
(15) J. W. Christian: *The Theory of Transformations in Metals and Alloys*, Pergamon Press, (1965), p. 489.
(16) P. C. Campbell, E. B. Hawbolt and J. K. Brimacombe: Metall. Trans. A, **22A** (1991), 2791.
(17) M. J. Lalich and C. R. Loper, Jr.: AFS Trans., **81** (1973), 238.
(18) D. Venugopalan: Metall. Trans. A, **21A** (1990), 913.